RESEARCH ARTICLE

ADVANCED FUNCTIONAL MATERIALS
www.afm-journal.de

Electro-Conductive Ti_3C_2 MXene Multilayered Membranes: Dye Removal and Antifouling Performance

*Zahra Zandi, Masoud Rastgar, Mojtaba Mohseni, Mostafa Dadashi Firouzjaei, Waralee Dilokekunakul, Babak Anasori, Chad D. Vecitis, Robert Keller, Matthias Wessling, Mark Elliott, Ahmad Rahimpour, and Mohtada Sadrzadeh**

This work describes the fabrication of a novel electroconductive membrane made of $Ti_3C_2T_x$ (MXene) nanosheet coating through a one-step pressure-assisted technique. Ti_3C_2-MXene is firmly attached over a polyamide–imide (PAI) microfilter by employing a binder composed of carboxymethyl cellulose (CMC)/glutaraldehyde (GA). Through coating a proper amount of multilayer Ti_3C_2-MXene, the electrical conductivity of 174 ± 0.16 S m^{-1} is achieved. The rejection rates of reactive red 120 (RR120), reactive black (RB), and methyl orange (MO) by the pristine PAI membrane are 45.2%, 40.81%, and 33.65%, respectively. However, rejection rates significantly improve with the Ti_3C_2 MXene coating to over 99.71%, 97.95%, and 68.91% for RR120, RB, and MO. Applying a 4 V cathodic potential resulted in a flux recovery ratio (FRR) of 99.83% and a flux decline rate (FDR) of less than 1% during humic acid (HA) filtration. Without applying voltage, the MXene-coated membrane shows an FRR and FDR of 92.51% and 45.56%, respectively. Surface energy analysis reveals strong repulsive interactions between foulants and the membrane surface. Moreover, the surface free energy indicates that foulants such as sodium alginate (SA) and bovine serum albumin (BSA) exhibit stronger adhesion to the membrane than HA, consistent with the fouling experiment results.

1. Introduction

Human beings are struggling with water-related challenges, including contamination and scarcity of freshwater resources.[1–3] To address such issues, researchers worldwide are actively exploring novel technologies that can efficiently eliminate contaminants from water while minimizing energy consumption.[4,5] In this context, implementing cost-effective and energy-efficient techniques for treating, recycling, and reusing industrial, agricultural, and domestic wastewater represents a practical approach toward achieving sustainable development for nations.[6] Among the various techniques being proposed thus far, advanced oxidation processes, such as the fenton reaction, ozone/UV, and photocatalysis, along with membrane-based technologies, stand out as highly promising approaches.[7] These techniques offer high treatment efficiency, minimal footprint, and versatility across

---

Z. Zandi, M. Rastgar, M. D. Firouzjaei, A. Rahimpour, M. Sadrzadeh
Department of Mechanical Engineering
10-241 Donadeo Innovation Center for Engineering, Advanced Water Research Lab (AWRL)
University of Alberta
Edmonton, AB T6G 1H9, Canada
E-mail: sadrzade@ualberta.ca

M. Mohseni, W. Dilokekunakul, R. Keller, M. Wessling
Chemical Process Engineering AVT.CVT
RWTH Aachen University
Forckenbeckstraße 51, 52074 Aachen, Germany

M. D. Firouzjaei, M. Elliott
Department of Civil, Construction, and Environmental Engineering
University of Alabama
Tuscaloosa, AL 35487, USA

The ORCID identification number(s) for the author(s) of this article can be found under https://doi.org/10.1002/adfm.202401970

DOI: 10.1002/adfm.202401970

M. D. Firouzjaei, B. Anasori
Department of Mechanical and Energy Engineering, Integrated Nanosystems Development Institute
Indiana University-Purdue University Indianapolis
Indianapolis, IN 46202, USA

B. Anasori
School of Mechanical Engineering
Purdue University
West Lafayette, IN 47907, USA

C. D. Vecitis
Harvard John A. Paulson School of Engineering and Applied Sciences
Harvard University
Cambridge, MS 02138, USA

M. Wessling
DWI – Leibniz-Institute for Interactive Materials
Forckenbeckstraße 50, 52074 Aachen, Germany

various water streams, often without the need for toxic chemical additives.[4] Recent advancements in the design and fabrication of novel membranes have positioned membrane technology as a superior option for water treatment compared to conventional methods.[8] However, sustainable membrane operations face significant technical hurdles, such as fouling, which must be addressed to ensure up-scaled feasibility.[9]

Membrane fouling, caused by the adsorption of undesired substances on the membrane surface or within its pores,[10] significantly hampers the performance and lifespan of membranes in separation technologies.[11] Consequently, addressing fouling challenges, especially in harsh environments, has become a critical and formidable task.[12,13] One approach to address membrane fouling is modifying the membrane surface using hydrophilic materials.[14] However, the achieved impact on fouling reduction during long-term operations remains insufficient.[15–18] To overcome this, researchers are delving into the development of advanced smart membranes[19,20] responsive to external stimuli such as pH,[21] temperature,[22,23] pressure,[24,25] ionic strength,[26] ultrasonication,[27] magnetic field,[28] and electric field.[29–31] Among these, the application of an electric field has garnered significant interest due to its precision and controllability. Recent studies have demonstrated that the accumulation of charged particles on the membrane surface can be adjusted by applying a constant electric potential to the electrically conductive membrane through electrostatic repulsion and electrochemical reactions, with the latter being more effective for organic fouling reduction.[32–36] Another mechanism involves electrochemical reactions that alter the molecular structure of foulants. Applying an electric potential to electroconductive membranes generates oxidizing species, such as hydroxyl radicals, that react with large macromolecular foulants, breaking them down into smaller compounds and thus preventing their attachment to the membrane surface.[32,33] Electromagnetic fields also play a role by modifying feed solution properties, such as pH and ionic strength, and disrupting foulant adhesion.[37–39] Furthermore, higher potential differences in electrochemical systems can induce water electrolysis reactions, generating oxygen and hydrogen gases. Gas bubbles on the membrane surface contribute to fouling mitigation by disrupting interactions between the membrane and foulants.[38]

Electroconductive membranes have been fabricated by depositing electrically conductive materials onto the surface of traditional membranes. Notable materials include copper,[40] nickel,[41] platinum,[42] indium tin oxide,[43] antimony tin oxide,[44] graphene,[32,33] and carbon nanotubes (CNTs),[45,46] applied through methods like electrophoretic deposition, plasma deposition, chemical vapor deposition, spin coating, chemical and electrochemical reactions, and layer-by-layer assembly.[47] Among these materials, 2D nanomaterials, particularly graphene, stand out for their conductivity and unique stacking structures that enhance selectivity for water solute removal. Integrating 2D nanomaterials into membranes holds promise for both conductivity and improved selectivity in water treatment applications.[46–48] MXenes, a recently discovered class of 2D nanomaterials,[49] has never been used to fabricate electroconductive membranes. The general MXene formula is $M_{n+1}X_nT_x$, where M represents elements such as Ti, Zr, and V,[50] interleaved with *n* layers of carbon or nitrogen (denoted as X), and T denotes surface terminal functions, e.g., O, OH, F, and/or Cl.[51,52] Multilayered Ti_3C_2 MXene, the most widely studied MXene,[48] exhibits high hydrophilicity, specific surface area, flexibility, mechanical strength, stability, and electrical and thermal conductivities, making it highly attractive for developing high-performance membranes for water purification.[53,54] Stacking 1-nm-thick 2D flakes of Ti_3C_2 MXene creates interconnected and densely packed nanochannels arising from relatively uniform interlayer spacings at the sub-nanometer scale within the laminar membranes.[55] This unique feature provides the membranes with a high surface-to-volume ratio and can significantly enhance the water/solute selectivity.[56–59] Furthermore, functional groups on Ti_3C_2 MXene 2D flake surfaces[60] enable covalent bonding, hydrogen dipole–dipole attractions, and electrostatic interactions between the host polymer and MXene nanostructures, facilitating uniform dispersion within composite membranes.[61] A remarkable feature is multilayered Ti_3C_2 MXene's high electrical conductivity (up to 24000 S cm^{-1}),[62] making it ideal for various electronic and energy-related applications.[51]

In this study, we successfully fabricated a novel Ti_3C_2 MXene-coated membrane using a simple pressure-assisted filtration technique. To enhance the chemical and mechanical stabilities of the MXene coating, carboxymethylcellulose (CMC) was incorporated into the MXene solution, followed by crosslinking the MXene/CMC coated membranes with the glutaraldehyde (GA) solution in the subsequent step. CMC, a polysaccharide derived from plant fibers, is characterized by its high water solubility and low cost. This biopolymer incorporates hydroxyl and sodium carboxymethyl groups ($-CH_2COONa$). Recognized for its advantageous attributes, CMC is valued for being biodegradable, nontoxic, highly hydrophilic, biocompatible, and possessing an exceptional ability to form films.[63] The Ti_3C_2 MXene-coated membrane exhibited remarkable improvements in rejection rates compared to the pristine polyamide–imide (PAI) membrane, achieving rejection rates exceeding 99.71%, 97.95%, and 68.91% for RR120, RB, and MO, respectively. We further demonstrated that the antifouling performance of the membrane could be easily enhanced by applying a low voltage between a multilayer Ti_3C_2 MXene-coated membrane and a stainless-steel electrode. By maintaining the desired level of antifouling performance, this membrane serves as a potential membrane platform capable of controlled fouling behavior. Surface energy analysis was also used to investigate the physicochemical interactions between foulants and the membrane surface during fouling experiments. This analysis provides valuable insights into the affinity and adhesion mechanisms governing fouling behavior and contributes to the development of effective membrane fouling control strategies.

2. Experimental Section

2.1. Materials

The etched multilayered Ti_3C_2-MXene powder was obtained from Luoyang Advanced Material Company (China). Carboxymethyl cellulose sodium salt (CMC), N,N-dimethylacetamide (DMAc, >99.9%), calcium chloride ($CaCl_2$), sulfuric acid (H_2SO_4), and acetone were provided by Fisher

Scientific. Also, polyvinylpyrrolidone (PVP, 360 kDa), poly (ethylene glycol) (PEG), triton X-100, glutaraldehyde (GA, 25 wt.% in water), humic acid (HA), sodium alginate (SA), glacial acetic acid (ReagentPlus, 99.0%), potassium hexacyanoferrate (III) ($K_4Fe(CN)_6$), and sodium nitrate ($NaNO_3$) were purchased from Sigma–Aldrich. PAI (Torlon 4000 THV) was supplied by Solvay Advanced Polymers. Reactive Red 120 (RR120, MW: 1774.15 Da), reactive black (RB, MW: 991.82 Da), and methyl orange (MO, MW: 327.33 Da) dyes were obtained from Sigma–Aldrich and utilized as organic contaminants in water. Bovine serum albumin (BSA) was purchased from ChemCruz. Fouling experiments were conducted on aqueous solutions of HA, SA/$CaCl_2$, and BSA. Deionized water was used throughout this research.

2.2. Membrane Preparation

2.2.1. Fabrication of PAI Support Layer

The fabrication of PAI support layers was carried out using the nonsolvent-induced phase separation (NIPS) technique. For this purpose, PAI polymer (Torlon 4000 THV), known for its exceptional thermal, mechanical, and chemical resistances, as well as superior hydrophilicity, was selected as the main polymer. PVP and PEG were employed as additives to optimize the membrane porosity. DMAc served as the solvent in this process. To prepare a homogeneous polymer solution, PAI (9 wt.%), along with the appropriate number of additives, was dissolved in the DMAc solvent. The mixture was stirred at a speed of 350 rpm and maintained at a temperature of 40 °C for 24 h. After stirring, the homogeneous solution was allowed to rest in a vacuum oven for 15 min to eliminate any air bubbles. Next, the PAI membrane layers were fabricated by using a film applicator to cast the solution onto a non-woven polyester fabric. The casting speed was set to 20 mm s^{-1}, and the gap height between the applicator and base plate was fixed at 120 μm. Finally, the cast film was submerged in a coagulation bath containing deionized water overnight to ensure the complete removal of the solvent from the polymer matrix.

2.2.2. Preparation of Ti_3C_2 MXene-coated PAI Membranes

To purify the MXene powder and remove impurities, 1 g of multilayered Ti_3C_2 MXene powder was washed three times. A stock solution of MXene was then prepared by suspending multilayer Ti_3C_2 MXene (1 g) in 50 mL of deionized water. The solution was then well-dispersed in a sonication bath for 1 h to effectively disintegrate MXene particle agglomerated and enhance the dispersion of MXene nanosheets in the coating solution. This stock solution was used to make the coating layer of each membrane. As shown in **Table 1**, three membranes with three different chemical compositions of the coating layer were prepared. CMC was utilized as a binder to establish a strong and durable attachment of Ti_3C_2 MXene layers to the PAI membrane surface. Three coatings were prepared by varying the amount of CMC binder and MXene (see Table 1). The evaluations revealed that 80 mg of MXene offered the highest electroconductivity due to optimal nanosheet overlapping, with a standardized supporting membrane area of 45.34 cm^2 chosen for consistent comparisons of different MXene concentrations in terms of electroconductivity and coating stability. At 4 mg, CMC exhibited negligible impact on membrane electroconductivity, enabling the attainment of a stable coating layer with an acceptable permeate flux. In all samples, deionized water was added to reach a total volume of 50 mL for the MXene coating solution. This coating solution was then subjected to sonication in a water bath for an additional 30 min. Next, each coating solution was passed through the microporous PAI membrane using a dead-end filtration cell, with a nitrogen gas pressure of 5 psi applied. Following filtration, the membrane was heat-treated in an oven at 50 °C for 15 min. Subsequently, the membrane was immersed in a 12 wt.% glutaraldehyde (GA) solution for 30 min to facilitate crosslinking. Finally, the Ti_3C_2 MXene-coated membrane underwent an additional 15 min of drying at 50 °C in preparation for further experiments. **Figure 1** shows the schematic illustration of the membrane fabrication process.

Table 1. Chemical composition of different coating layers of membranes.

Membrane ID	MXene [mg]	CMC [mg]	GA crosslinking time [min]
ECM1	80 mg	4	30
ECM2	40 mg	4	30
ECM3	40 mg	2	30

2.3. Physicochemical Characterizations of Membranes

Detailed information on the physicochemical characterization of membranes is provided in the Supporting Information. In summary, the hydrophilicity of the Ti_3C_2 MXene-coated PAI membranes was assessed using a contact angle analyzer. Membrane morphology was examined by field emission scanning electron microscopy (FESEM). The chemical bonding and elemental composition of the Ti_3C_2-MXene coating layer were elucidated using X-ray photoelectron spectroscopy (XPS), energy-dispersive spectroscopy (EDS), and Raman spectroscopy. Transmission electron microscopy (TEM) assessed the coating's thickness and integrity on the PAI substrate. The zeta potential of the samples was measured using an electrokinetic analyzer. The surface topography of the fabricated membranes was examined using atomic force microscopy (AFM). Finally, the leaching rate of titanium ions from the membrane samples was examined to evaluate the stability of the Ti_3C_2-MXene coating layer.

2.4. Membranes' Surface Energy Measurement

The surface energy of the ECM1 membrane was evaluated using the extended Young–Dupré and van Oss equation.[64] Based on the van Oss equation, the total surface tension $\gamma^{TOT}$of a medium can be expressed as the sum of the nonpolar (Lifshitz–van der Waals, γ^{LW}) and the polar (acid–base, γ^{AB}) surface tension components.[65] The polar acid–base component took into account the contribution of hydrogen bonding to the surface

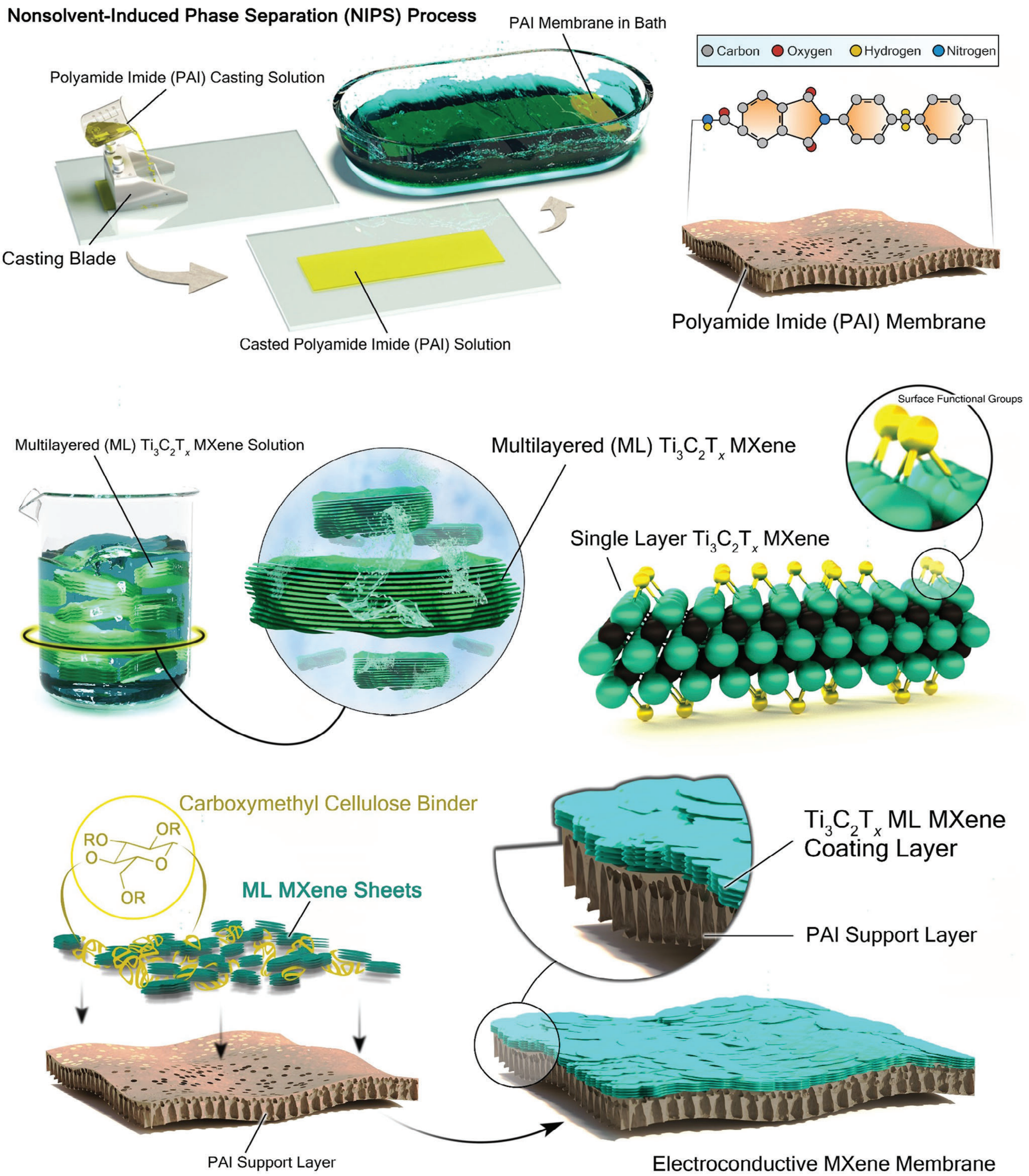

Figure 1. Schematic illustration of fabricating PAI and MXene-coated PAI electroconductive membranes.

tension component. The value of "γ^{TOT}" is calculated using the following equation:

$$\gamma^{TOT} = \gamma^{LW} + \gamma^{AB} \tag{1}$$

To implement this methodology, it was necessary to determine the surface tension components of both the membranes and the foulants using a three-probe liquid approach. The surface tension parameters for water, glycerol, and diiodomethane, with their corresponding nonpolar (Lifshitz–van der Waals) and polar (acid–base) surface tension components, can be found in Table S1 (Supporting Information).[65] First, the contact angles of three probe liquids (water, glycerol, diiodomethane), with known values of LW, negative (–), and positive (+) surface tension components, were measured.[64,66]

The measured contact angles were then substituted into Equation (2) to calculate the nonpolar (γ^{LW}) and polar (γ^{+} and γ^{-}) surface tension components of the solid surface.[66]

$$\gamma^{TOT}\left(1+\frac{\cos\theta}{r}\right) = 2\left(\sqrt{\gamma_s^{LW}\gamma_l^{LW}}+\sqrt{\gamma_s^{+}\gamma_l^{-}}+\sqrt{\gamma_s^{-}\gamma_l^{+}}\right) \tag{2}$$

where θ is the contact angle, s and l refer to a solid surface (membrane) and liquid, respectively. Superscripts LW, –, and + represent the nonpolar (Lifshitz–van der Waals), electron donor, and electron acceptor components of surface energy, respectively. Also, r is the Wenzel roughness factor, which represents the ratio of the actual surface area to the planar area. This factor is computed using the following equation.[67]

$$r = 1 + SAD \tag{3}$$

where SAD is the surface area difference and represents the percentage increase in surface area due to roughness. SAD value was obtained from AFM results. Also, the polar surface tension is made up of electron donor (–) and electron acceptor (+) components, which are calculated using the following equation.[64,66]

$$\gamma^{AB} = 2\sqrt{\gamma^{+}\gamma^{-}} \tag{4}$$

The nonpolar and polar surface tension components are used to calculate the nonpolar and polar free energy of adhesion between the membrane surface and different foulants using Equations (5) and (6), respectively.[64,66]

$$\Delta G_{mlf}^{LW} = 2\left(\sqrt{\gamma_l^{LW}}-\sqrt{\gamma_s^{LW}}\right)\left(\sqrt{\gamma_f^{LW}}-\sqrt{\gamma_l^{LW}}\right) \tag{5}$$

$$\begin{aligned}\Delta G_{mlf}^{AB} = {} & 2\sqrt{\gamma_l^{+}}\left(\sqrt{\gamma_s^{-}}+\sqrt{\gamma_f^{-}}-\sqrt{\gamma_l^{-}}\right)\\ & +2\sqrt{\gamma_l^{-}}\left(\sqrt{\gamma_s^{+}}+\sqrt{\gamma_f^{+}}-\sqrt{\gamma_l^{+}}\right)-2\left(\sqrt{\gamma_s^{+}\gamma_f^{-}}+\sqrt{\gamma_s^{-}\gamma_f^{+}}\right)\end{aligned} \tag{6}$$

Consequently, the total interfacial energy of adhesion between the membrane surface and foulants can be calculated by summing up the nonpolar and polar components of adhesion-free energy.[64,66]

$$\Delta G_{mlf}^{TOT} = \Delta G_{mlf}^{LW} + \Delta G_{mlf}^{AB} \tag{7}$$

In this study, water and glycerol were selected as polar liquids, while diiodomethane was used as a nonpolar liquid to calculate the polar and nonpolar surface tension components.

2.5. Membranes' Electrochemical Characterizations

To analyze the electrical conductivity of membranes, the resistance values of the Ti_3C_2-MXene coating layers were measured using a probe station in a four-point probe configuration. The prepared membranes were first cut into small pieces, and then a DC potential was applied to the dried surface of the membrane. The resulting current developed across the surface of the membrane was measured, allowing for the determination of resistance. Cyclic voltammetry (CV) and linear sweep voltammetry (LSV) experiments were conducted using a standard flow-through module generously provided by Flex-X-Cell GmbH for the purpose of electrolysis tests. The experimental setup employed a three-electrode configuration, wherein MXene-coated electroconductive membranes (5 × 5 cm^2) were designated as the working electrode, Pt-coated titanium expanded metal (4.5 × 5 cm^2) served as the counter electrode, and $Hg/HgSO_4$ saturated with potassium sulfate (−0.64 V vs SHE) was chosen as the reference electrode. A separation distance of 3 mm between the cathode and anode was upheld to maintain consistency, and the reference electrode was positioned external to the module within the inlet stream (see Figure S1, Supporting Information). The background electrolyte solution consisted of 100 mL of 50 mM Na_2SO_4, supplemented with 200 mg L^{-1} of the target foulants (HA, SA/CaCl2, and BSA). The module's flow rate was set at 50 mL min^{-1} throughout the experiments, and all CV and LSV measurements were conducted with a uniform scan rate of 15 mV s^{-1}.

2.6. Membranes' Permeation and Fouling Properties

The methodologies for measuring water flux, dye rejection, molecular weight cutoff (MWCO), and fouling tendency of membranes are outlined in the Supporting Information. The pure water flux was calculated using the following equation.[44]

$$J_w = \frac{\Delta m}{\rho A_m \Delta t} \tag{8}$$

where J_w is pure water flux, Δm is permeate mass, ρ is water density, A_m is the effective membrane surface area, and Δt is the filtration time. Dye rejection was determined by the following equation.

$$R\,(\%) = \left(1-\frac{C_p}{C_f}\right)\times 100 \tag{9}$$

where C_p and C_f, measured by UV–vis spectrophotometer, are the dye concentrations in permeate and feed solutions, respectively.

To evaluate the antifouling property of the membranes, the total flux decline ratio (FDR) and flux recovery ratio (FRR) were determined as follows:

$$\mathrm{FDR} = 1 - \frac{J_{wf}}{J_{w1}} \tag{10}$$

$$\mathrm{FRR} = \frac{J_{w2}}{J_{w1}} \tag{11}$$

where J_{w1} is the pure deionized water flux, J_{wf} is the permeate flux of the foulant solution, and J_{w2} is the pure water flux of the cleaned membrane. It is worth noting that, during the cleaning step, the membrane surface was subjected to the same DC electrical potential applied during the fouling step. While literature studies have shown that AC voltage is more effective in cleaning than DC, we applied DC voltage in this study to mitigate the oxidation and gradual dissolution of Ti.[68,69]

3. Results and Discussions

3.1. Characterization of Fabricated Membranes

The wettability of the membrane surface was assessed through water contact angle (WCA) and underwater oil contact angle (UWOCA) analyses. The surface roughness and chemistry of the membrane are crucial factors influencing wettability.[70,71] **Figure 2A** demonstrates that the initial WCA of the pristine PAI support was ≈41°, which reduced to zero within 30 s. Figure S2A (Supporting Information) shows that the pristine PAI support exhibited an average UWOCA of ≈124°. However, all Ti_3C_2 MXene-coated membranes displayed an apparent WCA of 0° immediately upon contact with water droplets. We did additional WCA analyses to distinguish the extent to which MXene and CMC contribute independently to the membrane's hydrophilicity. The surface of the PAI support layer was coated with either a CMC or MXene layer, and WCA measurements were conducted accordingly. The obtained results are presented in Figure S2B,C (Supporting Information). Coating of only CMC on the PAI support can slightly decrease WCA from 41° to 40°revealing its minimal contribution to the hydrophilicity of the fabricated composite membranes. CMC is generally considered a hydrophilic polymer; however, its relatively low concentration in the coating solution is unlikely to influence the overall hydrophilicity of the membrane significantly. In contrast, the membrane coated with only MXene demonstrated a WCA of 0°. Consequently, we can approve that the exceptional hydrophilicity of the MXene-modified membranes is attributed to the presence of hydrophilic functional groups on Ti_3C_2 MXene, enabling hydrogen bonding between Ti_3C_2 MXene and water molecules. Moreover, the UWOCA analysis of the ECM1 sample was conducted to assess the oil-repelling properties of the MXene-coated membrane. As depicted in Figure 2B, the oil droplet adhered to the surface of ECM1 when immersed in water. However, the droplet was removed from the surface upon pressure release and reverted to its original spherical shape, indicating easy separation from the membrane's surface. A similar investigation was carried out on the pristine PAI surface in DI water, and the results are illustrated in Figure S2D (Supporting Information). Following the pressure release in step 4, it was observed that the n-hexadecane droplet maintained adhesion to the PAI membrane surface. This suggests a higher affinity of the PAI membrane for nonpolar oil molecules.

The oil-repelling capability of the MXene-coated membranes under underwater conditions was evaluated using both light oil (n-hexane) and heavy oil (dichloromethane). As shown in Figure 2C and demonstrated in Movie S1 (Supporting Information), when the oil came into contact with the ECM1 surface, the light oil droplets were quickly expelled and floated on the water without adhering to the membrane surface. Similarly, when heavy oil droplets contacted the membrane surface (Figure 2D; Movie S2, Supporting Information), they formed spherical droplets that easily slid down to the bottom of the beaker. Consequently, upon removing the membrane from the bottom of the beaker, no noticeable oil adhesion was observed on the membrane surface, confirming the underwater oil-repelling behavior of the modified membrane. When a hydrophilic membrane comes into contact with water, the hydrophilic surface creates a thin hydration layer that acts as a solid–water interface.[72] This affinity is due to the presence of polar molecules or charged moieties mainly originating from MXene nanosheets (i.e., hydroxyl or carboxyl groups) on the hydrophilic membrane surface. As a result, oil interacts with the membrane–water interface rather than directly with the membrane surface, leading to reduced oil adhesion. Incorporating hydrophilic Ti_3C_2 MXene onto the PAI membrane facilitates the formation of the hydration layer, enhancing oil-repelling properties.

Figure S3A (Supporting Information) and **Figure 3**A_1,B_1,C_1 display the optical images of the pristine and MXene-coated membranes, respectively. The Ti_3C_2-MXene/binder nanocomposites are firmly attached to the yellowish surface of the PAI membrane without any visible detachment or pinholes. FESEM image of the top surface of the PAI support (Figure S3B, Supporting Information) reveals the membrane surface without any visible pores. The top FESEM images of the MXene-modified membranes (Figure 3A_2,B_2,C_2) confirm the successful coating of MXene particles made of 2D sheets of Ti_3C_2 MXene distributed over the modified membrane surface.

In Figure S3C (Supporting Information), the cross-sectional view of the PAI support layer demonstrates straight finger-like open pores that enhance membrane permeability by facilitating the passage of permeated water. SEM results show that the average thickness of the PAI support is ≈50 µm. The third column of Figure 3 presents the cross-sectional views of the MXene-modified membranes. The thickness of the MXene coating layer varied across different spots on the membrane surface, but its average thickness was ≈7 µm. To better observe the layered structure of the MXene nanosheets, the higher magnification FESEM images from ECM1 MXene coated surface are presented in Figure S4A (Supporting Information). EDX mappings were conducted in the same positions to assess the distribution of three elements: carbon (C), titanium (Ti), and fluorine (F) in the cross-sectional slicing of the membrane. The resulting EDX mapping images are shown in Figure 3. Carbon is present in both the PAI and MXene coating layers, while Ti and F are exclusively found in the top multilayer MXene layer. The EDX mapping images validate the deposition of MXene nanosheets across the membrane surfaces. The EDX spectra and the precise ratio of the

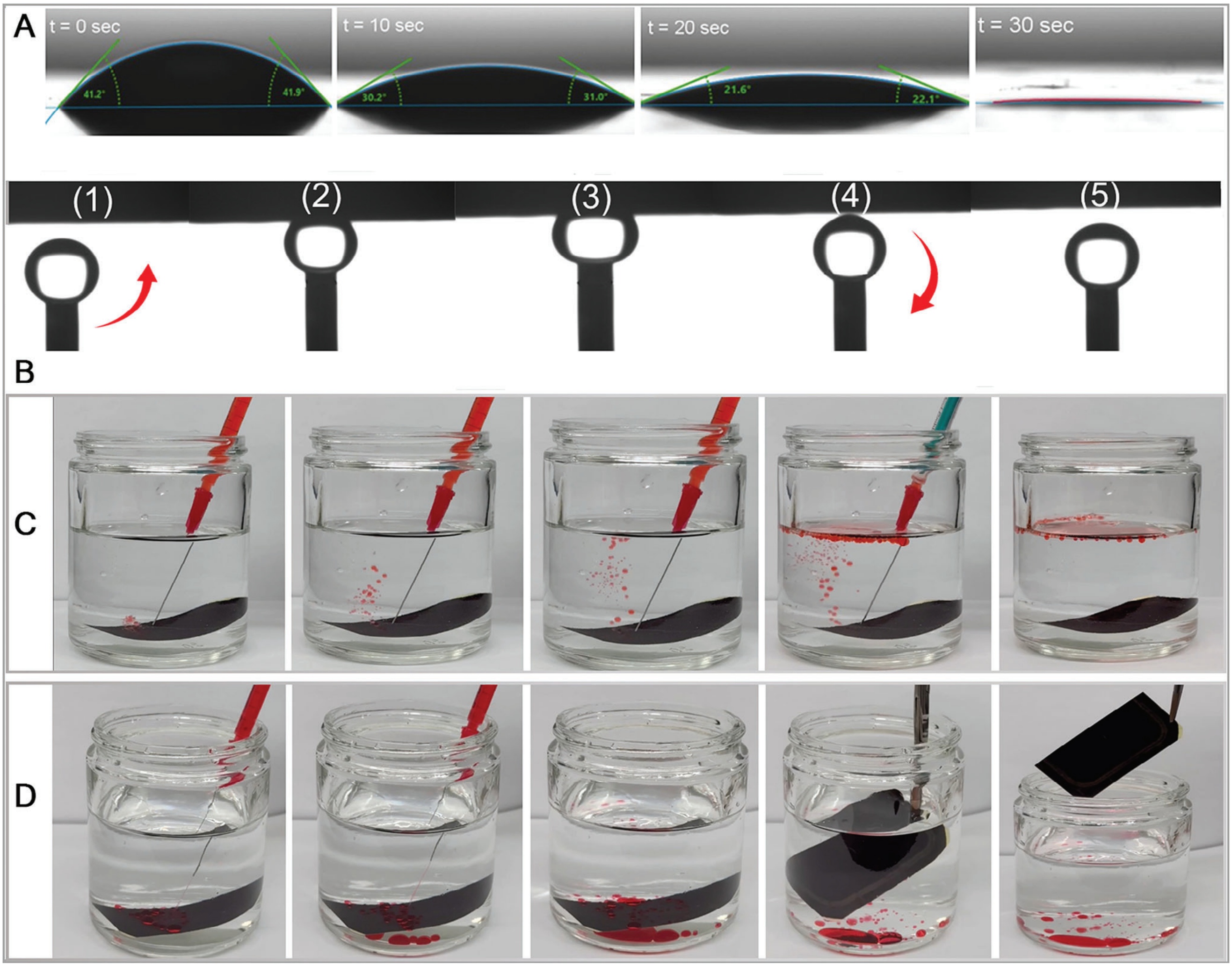

Figure 2. A) Dynamic water contact angles of pristine PAI membrane in 30 s. The initial WCA of the pristine PAI support is ≈41°, then drops to 0° in 30 s. All Ti_3C_2 MXene-coated membranes, on the other hand, exhibit an immediate WCA of 0° upon contact with water, which is attributed to hydrophilic functional groups on Ti_3C_2 MXene allowing strong hydrogen bonding with water molecules. The average UWOCA for the pristine PAI support is ≈124°. B) Different steps of n-hexadecane droplet interactions with the surface of ECM1 under DI water. Steps include (1) n-hexadecane droplet approaching, (2) touching, and (3) forcing to the ECM1 surface, (4) pressure release, and (5) full detachment of n-hexadecane droplet from the ECM1 surface. When immersed in water, oil droplets initially adhere to the membrane's surface but easily separate upon pressure release, returning to their spherical shape. C) the oil-repelling property of ECM1 in a light oil (n-hexane), fast repelling of the oil-injected droplets from the surface, and D) in a heavy oil (dichloromethane). Further testing of underwater oil repellence shows that both light (n-hexane) and heavy (dichloromethane) oil droplets are ejected from the ECM1 membrane surface. These droplets float on the water and form spherical shapes, confirming the modified membrane's exceptional underwater oil-repellency.

elemental composition of the membrane surfaces are reported in Figure S4B–D and Table S2 (Supporting Information).

Figure 4A presents TEM images of three different MXene-coated membranes. These images reveal the presence of accordion-like Ti_3C_2 particles on the surface of all three MXene-coated membranes, indicating the successful coating of multi-layered Ti_3C_2 nanosheets onto the PAI support. AFM was employed to assess the effect of MXene coating on surface roughness. Figure S5 (Supporting Information) shows 2D/3D AFM images of the pristine PAI support layer. The surface roughness values, including average roughness (R_{avg}), RMS roughness (R_{rms}), and Wenzel roughness ratio (1+SAD), are provided in Table S3 (Supporting Information). Upon MXene coating, R_{avg} and R_{rms} of the MXene nanocomposite membrane increased by more than fivefold from 35.89 and 45.05 nm for the pristine PAI membrane to 195.5 and 252.5 nm for ECM1. The reduction in MXene concentration in ECM2 and ECM3 resulted in greater MXene multilayer inhomogeneity and an increased number of surface cavities, increasing average roughness from 195.5 nm for ECM1 to 594.6 and 912.0 nm for ECM2 and ECM3, respectively. The Wenzel roughness, representing the ratio between the actual and projected solid surface area, increased from 1.384 for ECM1 to 1.885 and 1.813 for ECM2 and ECM3.

Figure 5A depicts the results of the zeta potential study conducted on the MXene-coated membranes and the PAI support at various pH values. The results show that the surface of the PAI

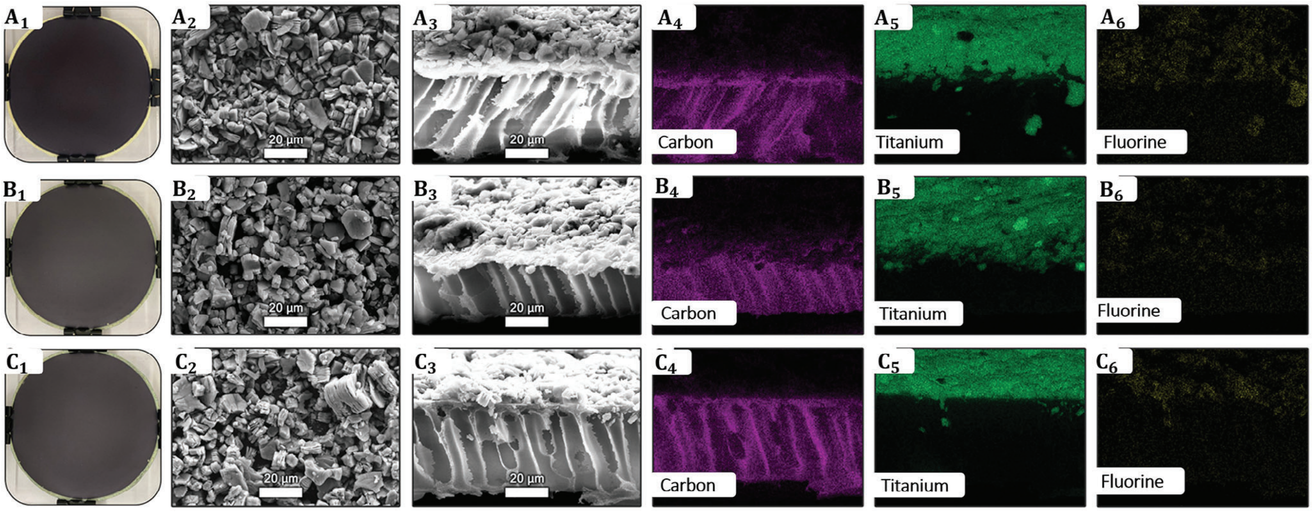

Figure 3. Physical appearance and morphological/elemental characterizations of the prepared MXene-coated membranes. A_1–A_6) show the characterization images of ECM1, B_1–B_6) for ECM2 and C_1–C_6) for EMC3. A_1, B_1, and C_1 show the optical depictions from the top surfaces of the fabricated Ti_3C_2 MXene-coated membranes. The second and third columns are top and cross-sectional FESEM images obtained from ECM1, ECM2, and ECM3 membranes. The three right columns demonstrate the EDX mapping analyses for three elements from the corresponding cross-section FESEM for each membrane.

support layer is negatively charged across the entire pH range, which can be attributed to the deprotonation of carboxyl and hydroxyl groups present on the surface. The negative charge density on the membrane surface was significantly enhanced upon coating the MXene layer on ECM1, ECM2, and ECM3. The negative charge of the MXene layer can be attributed to the presence of functional groups such as C═O, —OH, and —F, which carry negative charges.[48]

The electrical conductivities of the Ti_3C_2-MXene coating layers were measured using a four-point probe resistivity measurement (Figure 5B). ECM1 exhibited the highest electrical conductivity of 174 ± 0.16 S m^{-1} among all the prepared membranes. ECM2 and ECM3 coated membranes showed electrical conductivities of 27 ± 0.32 and 15 ± 0.13 S m^{-1}, respectively. The higher conductivity of ECM1 compared to those of ECM2 and ECM3 suggests that a higher amount of MXene (doubling the MXene amount) leads to an approximately tenfold increase in conductivity. This observed conductivity enhancement with a higher MXene coating can be attributed to the improved connectivity within the coating layer. A thicker coating with more MXene particles provides a more continuous conductive network between the particles with fewer gaps and voids, facilitating electron transport throughout the membrane. The higher conductivity of ECM1 implies that by adding more MXene, we can enhance the electrical conductivity, which is beneficial for our membrane use. However, increasing the MXene concentration will decrease the membrane flux because a denser MXene particle network could hinder the passage of molecules through the membrane. Thus, while a higher MXene coating thickness can enhance conductivity, practical considerations, such as flux reduction, must be considered when optimizing the MXene concentration. Figure S6 (Supporting Information) illustrates the dynamic electrical conductivity of ECM1 over 40 days of exposure to the ambient air.

The Raman spectra of the prepared Ti_3C_2-MXene membranes, including various modes with distinct vibrational frequencies, are shown in Figure 5C. The peak at 201 cm^{-1} wavenumber is specifically assigned to the A_{1g} (Ti, O, C) mode, which represents the out-of-plane vibrations of Ti atoms. The strong peak at 403 cm^{-1} corresponds to the E_g group vibrations of surface functional groups attached to Ti atoms.[73] Another characteristic peak exists at 617 cm^{-1} wavenumber, which relates to both E_g and A_{1g} vibrations of carbon.

Surface chemical compositions of the prepared membranes were investigated through XPS analyses, and the XPS survey scan spectrums are shown in Figure 5D. The important peaks corresponding to C 1s (≈284 eV), O 1s (≈455 eV), Ti 2P (≈532 eV), and F 1s (≈685 eV) of Ti_3C_2 MXene are marked on the plot.[74] The Ti concentration in all samples, as determined by XPS analysis, was ≈48 wt.%, a close match to the composition of the coating solution at ≈50%. The deconvoluted C 1s region for ECM1 is presented in Figure 5E. The prominent peak at a binding energy of 281.5 eV corresponds to the C—Ti—x bond, while the other two dominant peaks at 284.7 and 286.3 eV relate to graphitic C—C (or C—H) and C—O, respectively.[75] These chemical bonds exist in the structure of CMC and GA. Two smaller peaks centered at 287.5 and 289.2 eV correspond to the carbon bonds existing in the carbonyl and carboxyl functional groups, respectively. Similar deconvoluted peaks are observed for the C 1s region of ECM2 and ECM3 membranes, as shown in Figure S7 (Supporting Information).

The fractional percentage of each specific chemical bond was determined by measuring the peak area, and the resulting values for three different membranes are presented in Table S4 (Supporting Information). It is evident from the table that ECM1 exhibited the highest fraction of Ti—C—Ti, with a percentage of 14.28%. Figure 5F illustrates the Ti 2P region for ECM1, where the peaks at 455.5, 456.2, 457.3, and 458.0 eV can be attributed to Ti—C, Ti(II), Ti(III), and Ti(IV) or TiO_2, respectively.[76] Moreover, a prominent peak at 459.6 eV corresponds to $TiO_{2-x}F_x$ chemical bonds. The O 1s region of ECM1 was also analyzed through

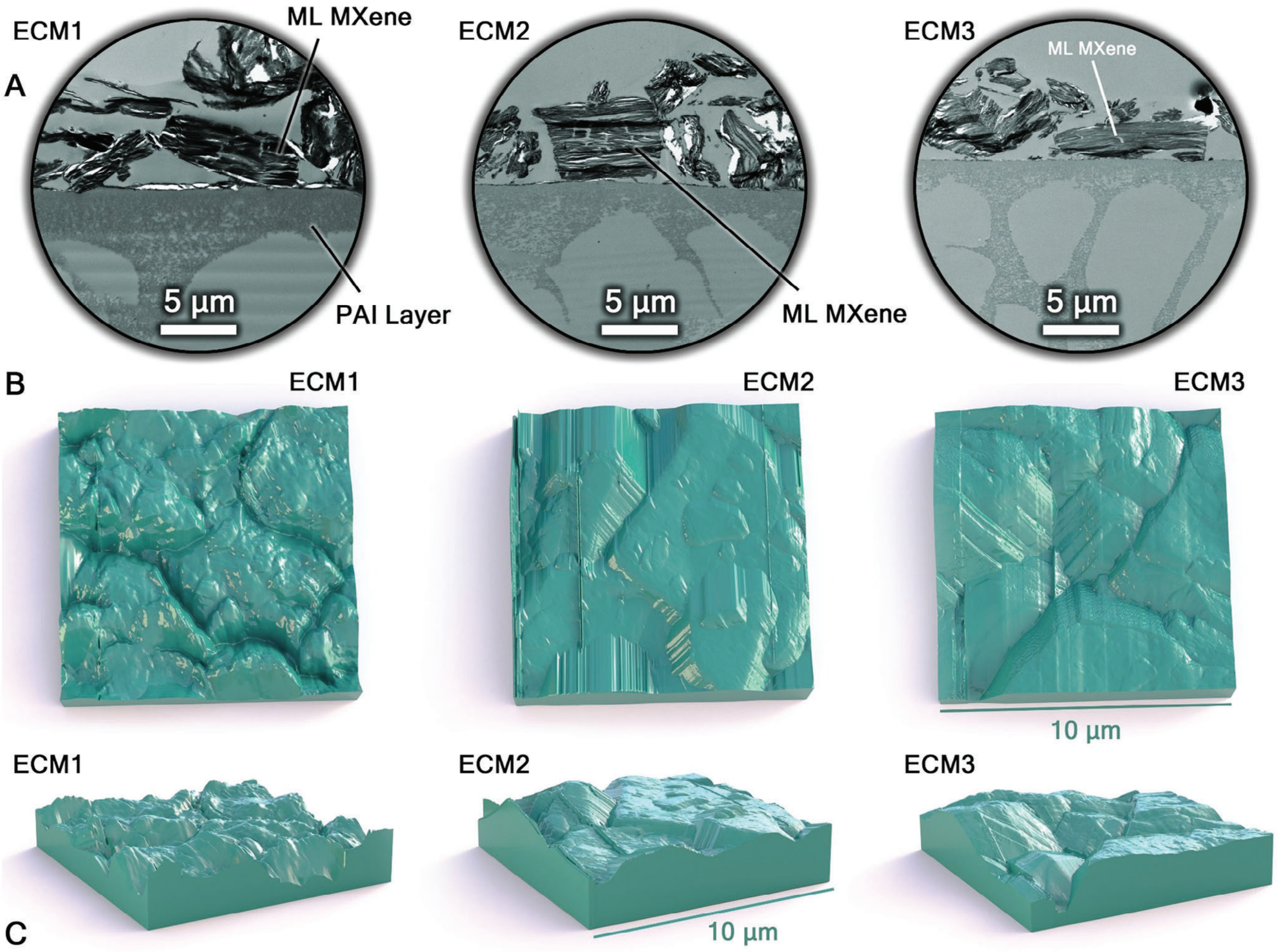

Figure 4. A) Cross-sectional TEM images for ECM1, ECM2, and ECM3, B) 2D AFM images of ECM1, ECM2, and ECM3, and C) 3D AFM images of ECM1, ECM2, and ECM3.

deconvolution, as shown in Figure 5G. This analysis revealed five fitting peaks at 530.0 eV (TiO_2), 530.7 eV (C—O), 531.9 eV (C=O), 533.9 eV (C—Ti—O or C—Ti—OH), and 534.2 eV (O—H).[77]

The physical stability of the modified membranes' coated layer was assessed by measuring the presence of Ti ions in the immersed solution. For this purpose, membranes with an effective surface area of 45.34 cm^2 were immersed in DI water and stirred at 100 rpm for three weeks.[43] The leaching rate of Ti ions served as an indicator of the stability of the Ti_3C_2 MXene coating layer. **Figure 6A** demonstrates the higher Ti leaching rate for the ECM1 membrane compared to the other two membranes (EC2 and ECM3). This observation could be attributed to the higher MXene content in the ECM1 membrane. The leaching rates for the first 7 days, first 14 days, and first 21 days are 0.029, 0.011, and 0.006 mg d^{-1}, respectively. Optical images of the membrane samples before and after three weeks of immersion in vigorously stirred water are provided in Figure S8 (Supporting Information), showing no visible detachment of particles on the modified membranes' surfaces. Furthermore, investigating the stability of the ECM1 in presence and absence of cathodic applied electric potential, revealed minimal differences in Ti release rates over 21-day period. The comparable stability observed in Ti release rates with applying potential and without applying potential underscores the robust performance of the membrane, emphasizing its resilience to potential-applied conditions (Figure S9 and Table S5, Supporting Information).

To evaluate the chemical stability of the modified membranes, various corrosive solutions and organic reagents (NaOH, HCl, ethylene glycol, and acetone) were employed. Optical images of the ECM1 membrane after 48 h of immersion in various pH solutions and organic solvents are presented in Figure S10 (Supporting Information). With the exception of the alkali solution with a pH of 13, all solutions appear clear, and no physical detachment can be observed on the surfaces of the tested membrane pieces. Exposure of MXene-modified membranes to harsh alkali solutions appears to weaken the covalent bonds between CMC and GA binders, leading to the peeling off of entrapped MXene nanoparticles from the PAI surface. The observed peeling of the coating layer indicates a challenge in maintaining the integrity of the modified membrane under highly basic conditions. Various strategies can be considered to mitigate the peeling phenomenon; however, it is crucial to recognize that these

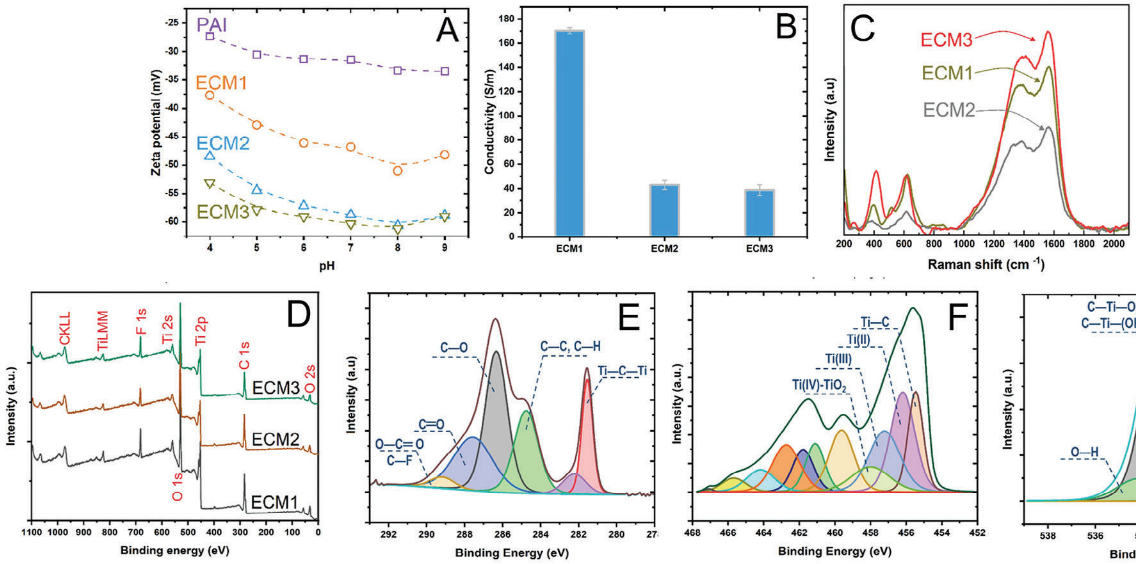

Figure 5. A) Surface zeta potential of M0 (pristine PAI membrane), ECM1, ECM2, and ECM3, B) electrical conductivity, C) Raman spectra, D) XPS survey scan of ECM1, ECM2, and ECM3, and high-resolution E) C 1s, F) Ti 2p, and G) O 1s for ECM1 membrane.

solutions may bring about specific side effects that can influence the overall performance of the membrane. For example, adjusting the concentration or composition of the binder (CMC/GA) to enhance the binding strength of the coating layer could potentially compromise the water permeability or electroconductivity of the fabricated membrane. Subsequently, the UWOCA of the ECM1 was measured after these experiments, and the obtained values are reported in Figure 6B. The MXene-coated membrane exhibited the UWOCA of ≈180° after 48 h of immersion in acetone and ethylene glycol solutions. A similar UWOCA was measured for the ECM1 membrane after immersing it in an HCl acid solution.

3.2. Dye Separation Performance of Ti_3C_2 MXene Modified Membrane

The water flux and dye rejection performance of PAI and all modified membranes were assessed using a crossflow filtration setup. As shown in Figure 6C, coating the membrane surface with Ti_3C_2-MXene resulted in a decline in water flux from 1400 LMH to 57 LMH, 80 LMH, and 140 LMH for ECM1, ECM2, and ECM3, respectively, at 20 psi transmembrane pressure. However, the efficacy of the membrane in dye rejection significantly increased. The performance of all fabricated membranes for rejecting three different dyes, namely RR120 (MW: 1774.15 Da), RB (MW: 991.82 Da), and MO (MW: 327.33 Da), was evaluated.

The chemical characteristics of these dyes are provided in Table S6 (Supporting Information). Based on the experimental results shown in Figure 6D, the coating of the MXene layer on the ECM1 membrane surface improved the dye rejection performance from 45.2% to 99.71% for RR120, from 40.81% to 97.95% for RB, and from 33.65% to 68.91% for MO. Optical images of the feed solutions for the three different dyes, as well as the permeated solutions passed through ECM1, are displayed in Figure 6E.

The coating of Ti_3C_2 MXene followed by CMC/GA crosslinking effectively reduced the membrane surface pore size (≈20 times), as evidenced by the MWCO and flux results (Figure 6C,F), leading to enhanced dye rejection. Three important factors can influence the dye separation capacity of the fabricated membrane.

3.2.1. Membrane Pore Size

It is conceivable that the higher concentration of Ti_3C_2 MXene on ECM1 might reduce its pore size and surface cavities compared to the other two fabricated membranes, resulting in more effective dye rejection by ECM1. Comparing the dye rejection results between ECM2 and ECM3, it can be concluded that the concentration of CMC as a binder can also impact the membrane pore size, which can be manifested in dye separation performance. Reducing the CMC concentration in ECM3 led to a slight decline in membrane dye rejection performance.

3.2.2. Membrane Surface Charge

The electrostatic repulsion between negatively charged dye molecules and the negatively charged modified membrane surfaces emerges as a crucial contributing factor to the increased dye rejection. Ti_3C_2 MXene possesses a high density of negatively charged functional groups on its surface, which results in a negatively charged MXene layer on the membrane surface, as evidenced by zeta potential measurements (see Figure 5A). Dye molecules, such as RR120, RB, and MO, often exhibit negatively charged groups, either intrinsically or due to their dissociation in water. As these negatively charged dye molecules approach the modified membrane surface, a strong electrostatic repulsion between the like charges hinders their penetration through the membrane. This repulsion acts as a barrier, preventing the

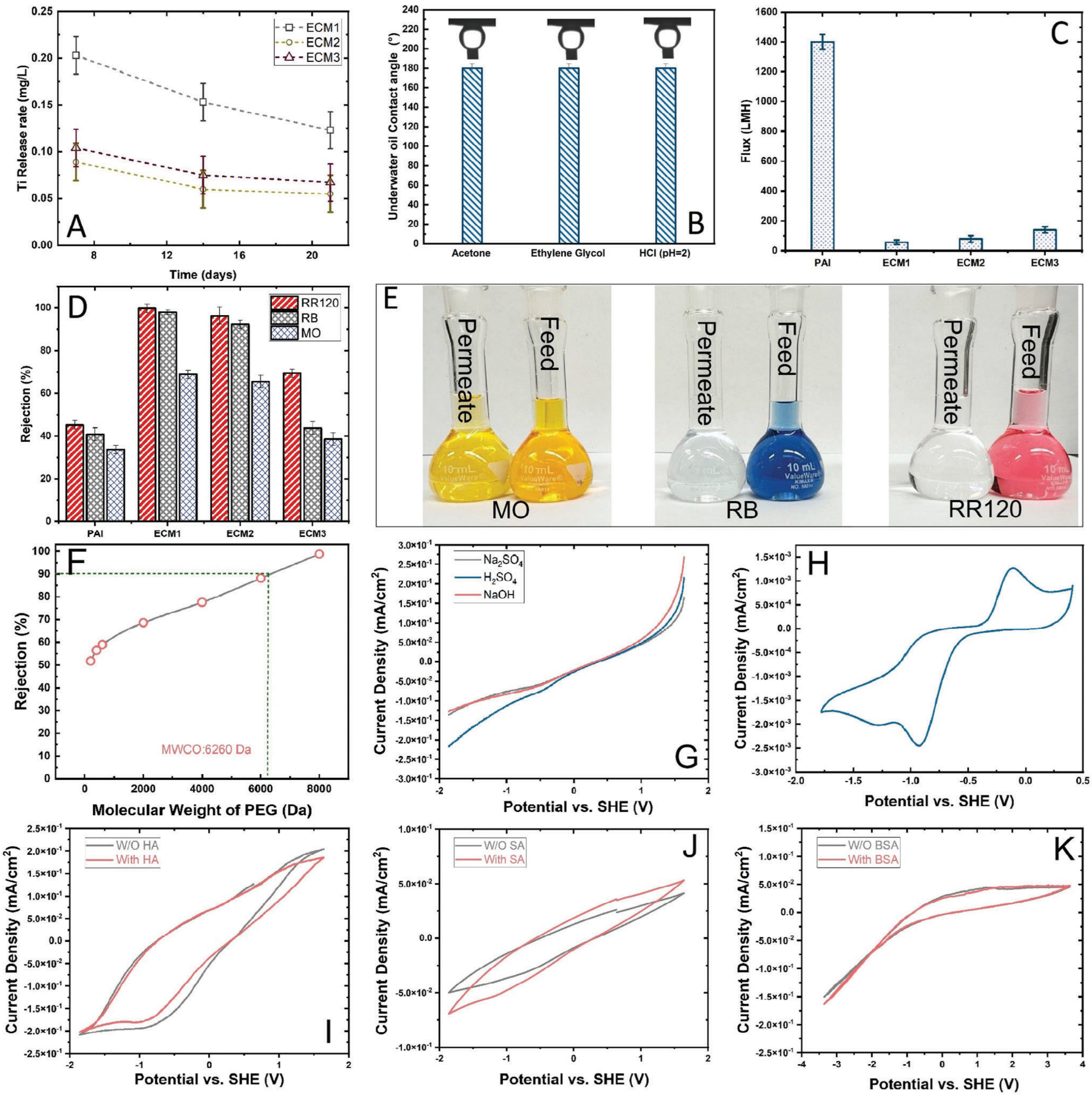

Figure 6. A) The concentrations of Ti from the surfaces of three different membranes in the immersed solutions. The samples were taken on different days, and the released Ti concentration was measured through the ICP method. B) UWOCA of the ECM1 after 48 h immersion in acetone, ethylene glycol, and HCl acidic solution. C) pure water flux, and D) RR120, RB, and MO dye rejection performances of all synthesized membranes. E) Optical images of ECM1 membrane performance in the rejections of three different dyes: the right flasks are the feed, and the left flasks are the permeate solutions. F) MWCO for the ECM1 membrane, G) LSV, and CV curves of ECM1 membrane H) in the mixture of $K_4Fe(CN)_6$ (0.01 M)/$NaNO_3$ (0.1 M) solution with a potential range from −1.77 to 0.41 V versus SHE with a scan rate of 15 mV sec^{-1}. I–K) CV curves for the ECM1 in the lack and presence of different model foulants with different potential ranges.

passage of dye molecules through the modified membrane, consequently leading to increased dye rejection percentages. The effectiveness of this electrostatic repulsion mechanism is influenced by the MXene concentration, as demonstrated by the varying rejection performances of ECM1, ECM2, and ECM3.

3.2.3. Thickness of Coated Layer

The thickness of the coated layer plays a crucial role in determining the diffusion path length for dye molecules during separation. While a thicker coated MXene layer may negatively impact water permeability, it creates a tortuous path for the dye-contaminated solution. Consequently, optimizing the nature and strength of the interaction between the selective membrane layer and dye molecules can enhance membrane selectivity. This is evident in TEM images, as Figure 4A clearly illustrates that ECM1 has a thicker coated MXene layer.

MWCO experiments were conducted on the ECM1 using 200 ppm of PEG with different molecular weights, and the data obtained is illustrated in Figure 6F. The results reveal that the MWCO of the ECM1 membrane is ≈6200 Da, indicating that the membrane can reject>90% of solutes with a molecular weight of this magnitude. Since the molecular weights of the studied dyes are significantly lower than 6,200 Da, it was expected that the membrane would have a very low rejection capacity for these dyes. It is important to note that while MWCO indicates the membrane's sieving capability based on size, it does not fully capture the complex interactions between the membrane and the dye molecules, which can affect rejection performance. Membrane surface interactions due to surface charge, hydrophilicity/hydrophobicity, presence of functional groups, and electrostatic interactions can contribute to dye rejection.[78–81] Therefore, MXene-coated membranes, specifically ECM1 with higher amounts of MXene, showed a high rejection rate even for dyes with molecular weight lower than 6200 Da.

It is worth mentioning that the molecular separation efficiency of MXene-coated membranes fabricated in this study still lags state-of-the-art nanofiltration membranes. This limitation can indeed be attributed to the multilayered structure of the MXenes integrated into the coating layer, resulting in non-selective spaces or gaps between individual MXene layers.[82] This architectural feature, inherent to the multilayered structure, may have significant implications for the observed lower rejection rates.

Figure 6G illustrates the electrochemical assessment of MXene-coated membranes within a flow-through electrochemical cell, utilizing LSV methodology. The current response indicates an incremental trend in all three electrolytes as the potential decreases, indicative of the hydrogen evolution reaction (HER). However, the attained current response remains modest, peaking at a maximum value of -0.22 mA cm^{-2} with an applied potential of -1.9 V versus SHE in an H_2SO_4 solution. Among the tested electrolytes, i.e., NaOH, Na_2SO_4, and H_2SO_4, the latter establishes a more conducive milieu for HER due to its higher proton concentration. The LSV outcomes showcase the conductivity and operational efficacy of the in-house fabricated membranes functioning as electroconductive substrates.

Cyclic voltammetry tests were performed to assess the electrochemical activity of the Ti_3C_2-modified membranes in reduction and oxidation processes. As shown in Figure 6H, the ECM1 membrane exhibited two prominent peaks related to redox reactions when exposed to potassium hexacyanoferrate. The cathodic and anodic peaks at ≈-0.92 V and -0.1 V, respectively, versus SHE, correspond to the reduction and oxidation of the $Fe(CN)_6{}^{3}$-/$Fe(CN)_6{}^{4}$- redox pair species. The observed peak currents for both the cathodic and anodic peaks indicate the electrochemical activity of the Ti_3C_2 MXene membrane surface.

Furthermore, three additional CV tests were conducted using ECM1 as a working electrode in the presence of model foulants, and the results are depicted in Figure 6I–K. All these CV results indicate no significant difference between the voltammogram of the baseline electrolyte (Na_2SO_4) and those infused with 200 mg L^{-1}. As depicted in Figure 6I,J, neither SA nor HA engages in discernible interactions with the MXene-coated surface within the range of applied potentials (-1.9 V to 1.6 V versus SHE). The CV data for BSA (Figure 6K) spans an expanded potential spectrum: -3.3 to 3.6 V versus SHE. However, similar to the behavior of HA and SA, BSA exhibits no distinct peaks corresponding to reduction or oxidation in comparison to the background electrolyte.

3.3. Study of Membrane's Fouling Behavior in an Electrochemical Cell

The fouling potential of the MXene-modified membrane (ECM1) and its corresponding flux recovery ratio (FRR) were assessed through three-step dynamic crossflow filtration experiments with feed solutions containing HA, SA/CaCl2, and BSA. To evaluate the impact of the electric potential application on the membrane's FDR and FRR in the fouling tests, distinct cathodic potentials were applied, and the normalized water flux versus time was recorded. **Figure** 7A illustrates the water flux through the ECM1 membrane for the HA solution over time, aiming to evaluate the organic fouling. When negative potentials of 2 and 4 V were applied to the ECM1 membrane surface, the FRR increased from 92.52% to 95.63% and 99.83%, respectively. Simultaneously, the FDR decreased from 45.56% to 23.13% and <1% with the application of 2 and 4 V negative potentials, respectively. These results demonstrate that the antifouling property of the ECM1 membrane significantly improved with higher negative potentials applied.

The MXene-modified membrane's performance in resisting organic fouling was further evaluated using a feed solution containing sodium alginate and calcium chloride in the same three consecutive steps as before. Figure 7B (right side) illustrates that by applying -6 V potential, the FRR increased from 84.74% to a maximum value of 99.94%, while the FDR decreased significantly to a minimum value of <1%. These results indicate that the ECM1 membrane experienced no fouling with SA/$CaCl_2$ as the applied cathodic potential was increased from 0 to 6 V. In addition to the benefits of the electric field in reducing membrane fouling, we also observed a high flux recovery rate for membranes subjected to a negative voltage after membrane washing. Similarly, Figure 7C, left side) shows a substantial reduction in the fouling propensity of ECM1 under the negative voltages (2, 4, 6, and 8 V) during the filtration of a BSA solution. Applying an 8 V electric field in the electrochemical cell (Figure 7C) resulted in >99% FRR and an almost negligible FDR, indicating excellent protein fouling resistance of MXene-modified membranes. In the BSA fouling tests, utilizing the most challenging fouling material for the fabricated membranes, the total energy consumption per area $\left(\frac{KWh}{m^2}\right)$ was determined by applying an 8 V potential to counteract fouling effects effectively. The calculation, expressed as $\left(\frac{\text{Applied potential }(V)\times\text{Current }(A)\times\text{Time }(h)}{1000\times\text{membrane active surface area}}\right)$, yielded a requirement of 0.1698 $\frac{KWh}{m^2}$ of electrical energy to mitigate protein fouling.

Overall, Figure 7 indicates that the initial stage involves a rapid decline in flux within the first 5 min, followed by a subsequent phase where the flux decline stabilizes into a steady-state pattern. This two-stage fouling mechanism suggests a dynamic

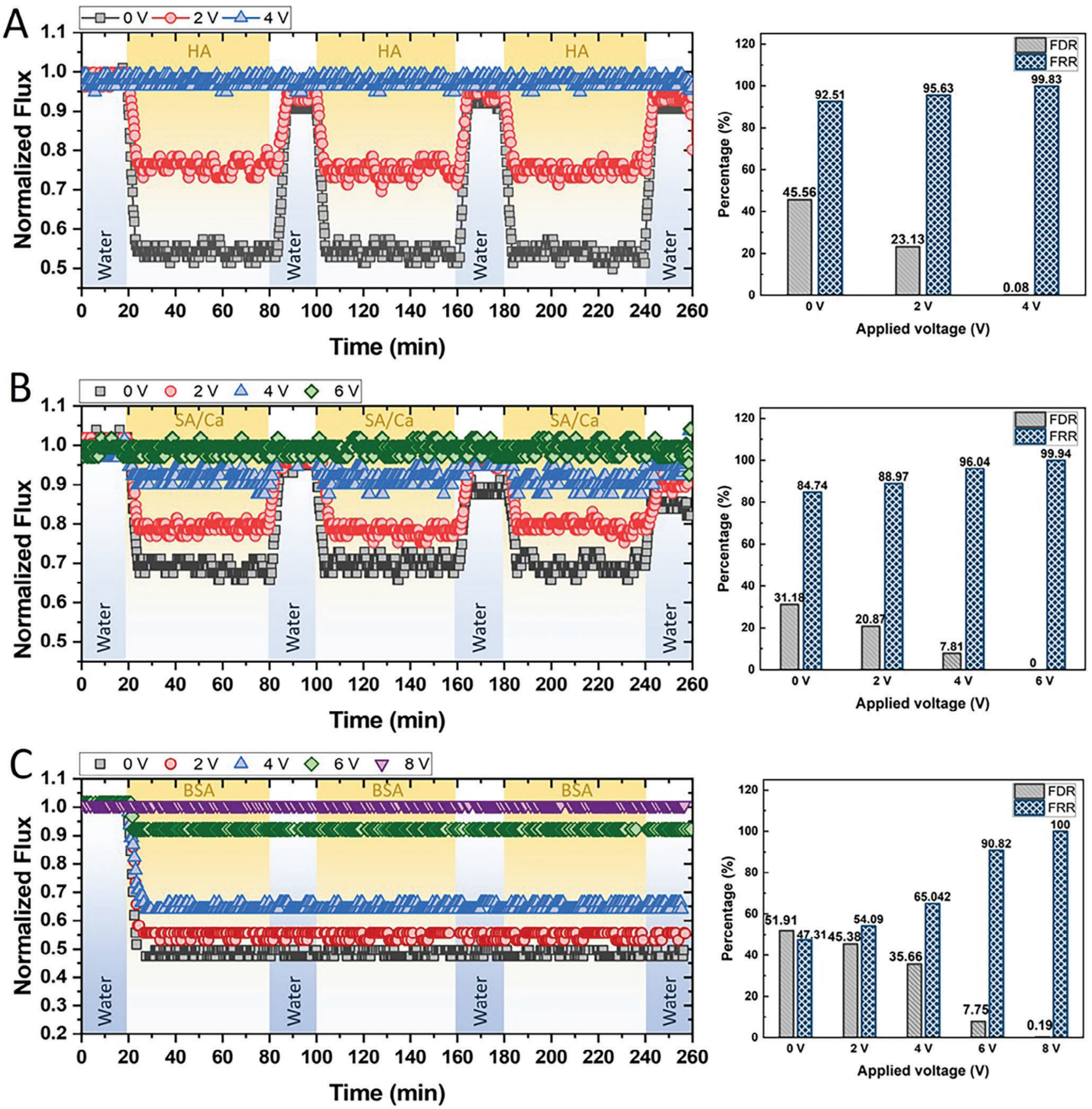

Figure 7. Variation of normalized water flux versus time for prepared ECM1 with different applied voltages using various foulant solutions (left side) with corresponding FDR and FRR values (right side): (A) HA solution (200 ppm HA, pH≈7), (B) SA/CaCl$_2$ solution (200 ppm SA and 0.5 mм CaCl$_2$), and (C) BSA (200 ppm).

fouling process where an immediate and intense fouling effect takes place initially, likely due to the accumulation of larger particles or the formation of a surface layer. This is then succeeded by a more gradual fouling process that establishes a consistent flux reduction rate. The primary fouling mechanism can be inferred from this observation. The abrupt flux decline in the early stage implies that particulate fouling, where larger particles block the membrane pores or attach to its surface, might be the dominant mechanism during this period. As the flux decline stabilizes in the later stage, it could indicate that a secondary fouling mechanism, such as cake formation or concentration polarization, starts to play a more substantial role in contributing to the flux reduction.

The observed enhancement in fouling resistance can be attributed to multiple factors. First, the strong electrostatic repulsion between the membrane and the foulants, along with the

Table 2. Surface energy parameters (mJ m^{-2}) of ECM1 and studied foulants.

Membrane/ Foulants	γ^{LW}	γ^{+}	γ^{-}	γ^{AB}	γ^{TOT}	ΔG^{LW}_{mlf}	ΔG^{AB}_{mlf}	ΔG^{TOT}_{mlf}
ECM1	37.68	0.76	34.44	10.23	47.91	–	–	–
HA[a)]	47	0.3	43	−2	40	−6.42	19.97	13.54
SA/CaCl$_2$[a)]	46	2.1	40	−4	15	−6.21	16.55	10.33
BSA[a)]	49	2.4	27	−6	7	−6.85	6.95	0.10

[a)] Adapted from "Assessment of physicochemical interactions in hollow fiber ultrafiltration membrane by contact angle analysis", by Nashida Subhi et al., Journal of Membrane Science, 403–404.[85]

occurrence of electrochemical reactions, play significant roles, as will be elaborated later. The negatively charged contaminants in the water, including HA, SA, and BSA, are effectively repelled from the membrane surface due to the negative charge on the cathode surface, resulting in highly effective electrostatic repulsion forces. Moreover, the potential direct and indirect electrochemical reactions occurring on the membrane surface might also contribute to the degradation of organic matter and reduce its adherence to the membrane surface, primarily by diminishing hydrophobic attraction. Additionally, the fabricated membranes exhibit remarkable superhydrophilic properties, as indicated by WCA results. Consequently, when immersed in aqueous solutions, a hydration layer forms on the surface of ECM1 due to the affinity of water molecules. This hydration layer further minimizes interactions between the membrane surface and foulants, thereby enhancing fouling resistance. These factors collectively contribute to the observed fouling resistance, either due to inherent static membrane properties (e.g., wettability) or applied potential (e.g., electrostatic repulsion forces). They showcase the intricate interplay between high electrostatic repulsion forces, possible negligible electrochemical reactions, and the superhydrophilic properties of the fabricated membranes, ultimately leading to improved fouling resistance.

To quantitatively compare the fouling phenomenon through different model foulants, an empirical exponential flux model, $J_t = J_0 \exp(-kt)$, was employed.[83,84] In this equation, J_t represents the permeability at time t (h), J_0 denotes initial permeability at time = 0, and k (h^{-1}) is the fouling rate constant. It is important to note that we kept all hydraulic conditions, including spacers and flow rate, constant across all fouling experiments. Therefore, the reduction in fouling rate can only be attributed to the type of foulant and the applied electric potential. As illustrated in Figure S11 and Table S7 (Supporting Information), for lower potentials (0 and 2 V), R^2 values exceed 0.9, indicating a robust fit to the pseudo-first-order kinetic model for all foulants. However, as higher potentials (4, 6, and 8 V) were applied, lower R^2 values were obtained, suggesting minimal time-dependent fouling.

3.4. Surface Free Energy

In fouling experiments, the deposition of foulants on the membrane surface is typically influenced by both hydrodynamic and physicochemical interactions between the foulant macromolecule and the membrane surface.[85] However, the physicochemical interactions are found to be more influential in the membrane fouling phenomenon.[66,86] The surface tension components of a membrane provide valuable insights into the energy associated with the affinity between the membrane surface and foulants with varying chemistry and molecular structures. Contact angle analyses were performed to determine these surface tension components using three probe liquids with different polarities: water, glycerol, and diiodomethane. The recorded contact angles for these liquids were 0°, 18°, and 0°, respectively. As shown in Table 2, the obtained surface tension components indicate that all the studied foulants and the membrane possess high electron donor monopolarity and negligible electron acceptor components.[87] This finding aligns with the characteristics of polymeric membranes, which are often characterized by high electron donor monopolarity.[66] Also, the monopolar surface properties of all model foulants observed in this study are in line with previous findings reported by Subramani et al.[88]

The free energy of adhesion represents the energy per unit area between the membrane surface and foulants when submerged in a solvent, such as water. If $\Delta G^{TOT}_{mlf} > 0$, the membrane surface is considered hydrophilic and exhibits a higher affinity for water than foulants. Conversely, if $\Delta G^{TOT}_{mlf} < 0$, the attachment of foulant molecules is more favorable.[89] Table 2 shows that ECM1 has a higher electron donor compared to electron acceptor surface tension components, suggesting that the basic component of the acid–base (AB) interactions controls the polar contribution of the surface free energy. Additionally, for ECM1, the nonpolar components contribute significantly to the total surface tension. Given the relatively large negative values of the foulants, these materials are expected to exhibit repulsive behavior when deposited on the membrane surface.[90] The significantly high positive value of ΔG^{TOT}_{mlf} (13.54 mJ m^{-2}) for HA reported in Table 2 indicates that the interactions between the membrane and HA molecules are expected to be strongly repulsive. Also, based on the calculated ΔG^{TOT}_{mlf} values for SA and BSA, it is expected that these foulants exhibit relatively stronger adhesion to the membrane surface compared to HA, as the interfacial adhesion energy between the membrane and SA or BSA foulants is lower than that of HA.

In conclusion, by applying an external electric potential, the loosely attached HA foulants to the membrane surface can be effectively removed after washing, restoring the water permeation performance to its initial value. The membrane fouling behaviors depicted in Figure 7 confirm the findings of this study, where a complete antifouling performance was observed during lower cathodic potential applications in the HA experiments. It's important to note that while the thermodynamics described by ΔG provides insights into the potential adhesion strength, other factors such as the kinetics of the adhesion process, fouling dynamics, and the presence of external factors (e.g., flow rate, shear forces) should also be considered to obtain a comprehensive understanding of fouling behavior.

3.5. Mechanisms of Fouling Mitigation in Ti_3C_2-MXene Modified Membranes

Electrostatic repulsive forces play a significant role in mitigating fouling between the negatively charged membrane and negatively charged foulants. Since all the studied foulants possess a negative intrinsic surface charge,[91] applying an external potential to increase the negative charge on the membrane surface enhances the electrostatic repulsion between the membrane surface and foulants, thereby minimizing foulant attachment. Previous studies have demonstrated that manipulating surface charge can effectively regulate organic fouling by reducing pore blocking and gel formation.[92] Observations indicate that the repulsive force between the membrane surface and foulants increases as the cathodic potential increases. Consequently, foulant attachment to the membrane is further reduced, improving overall antifouling performance. Moreover, the application of an electric field between external electrodes has been shown to enhance the antifouling propensity of the membrane.[93] This can be attributed to the electrophoresis phenomenon, where charged foulant particles in water experience movement under the influence of the electric field toward the electrode with the opposite charge, preventing foulant deposition and cake layer formation on the membrane surface.

Gas bubbling represents another effective mechanism for controlling membrane fouling.[94] During conventional reduction/oxidation processes on inert electrodes, water electrolysis can occur, leading to the hydrogen evolution reaction (HER) and oxygen evolution reaction (OER) on the electrode surfaces. The HER involves the oxidation of water molecules to form oxygen gas on the anode surface (Equation 12). Additionally, water electrolysis generates hydrogen bubbles on the cathode surface (Equation 13). By increasing the electric potential, the production of hydrogen gas on the electrode surface can be augmented, which mitigates the fouling rate.

$$2H_2O \rightarrow O_2 + 4H^+ + 4e^- \tag{12}$$

$$2H_2O + 2e^- \rightarrow H_2 + 2OH^- \tag{13}$$

Furthermore, electrochemical reactions may occur on the membrane surface regardless of the process configuration. Electrochemical reduction involves two cathodic processes. The first process, known as direct electron transfer (DET), involves the transfer of electrons from the cathode surface to the foulants. However, based on the CV results, the observed antifouling performance of the fabricated Ti_3C_2 MXene multilayered membranes cannot be attributed to the DET mechanism, as no corresponding reduction peak was observed within the applied potential range. The second process is an indirect electrochemical reduction mechanism induced by atomic hydrogen (H^*) adsorbed on the cathode surface. By applying a cathodic potential, atomic hydrogen might also be generated on the membrane surface (cathode) through the electrochemical reduction of protons (H^+) in the electrolyte (Equation 14).[95] In the indirect electroreduction process, the adsorbed atomic hydrogen interacts with the foulants, leading to their reduction. The adsorption of atomic hydrogen on the membrane surface can facilitate foulant reduction through various mechanisms. One possible mechanism involves the reaction of atomic hydrogen with foulants present in the electrolyte, breaking their chemical structure. This reaction, known as hydrogenolysis, involves the cleavage of chemical bonds in foulant molecules by atomic hydrogen, leading to the formation of smaller, less complex molecules that can be easily removed from the system.[96,97]

$$H_2O + e^- \rightarrow H^* + OH^- \tag{14}$$

Another mechanism for mitigating fouling is the generation of superactive reagents, such as hydroxyl radicals ($^\bullet OH$), which can attack the chemical bonds of organic compounds near the membrane surface. This process reduces the molecular size of organic foulants and weakens their attachment to the membrane surface by diminishing hydrophobic interactions.[98] Also, during the cathodic reaction, electrons are transferred from the cathode to dissolved oxygen molecules in the surrounding solution. In acidic solutions, this results in the reduction of O_2 to form hydrogen peroxide, H_2O_2, at the cathode surface (Equation 15).[99,100] In neutral pH solutions, the reaction still occurs but at a slower rate compared to acidic media. In alkaline solutions, electrons are transferred from the cathode to oxygen molecules in the solution, leading to the reduction of O_2 and the formation of hydroperoxide ions (HO_2^-) and hydroxide ions (OH^-) (Equation 16).[100]

$$O_2 + 2H^+ + 2e^- \rightarrow H_2O_2 \tag{15}$$

$$O_2 + H_2O + 2e^- \rightarrow HO_2^- + OH^- \tag{16}$$

4. Conclusion

This study presented a method to develop physically stable electro-conductive membranes with great robustness in vigorous stirring conditions. Specific weight ratios of MXene and CMC were co-deposited onto PAI support using pressurized air force to make electroconductive membranes that could respond to changes in an electric field. The primary objective of this study is to evaluate the efficacy of Ti_3C_2 MXene-based membranes for water treatment. To accomplish this, we employed a straightforward pressure-assisted filtration method known for its controllability in adjusting the thickness of the coated layer. Nevertheless, alternative practical techniques such as spraying, film casting, and dip-coating can be considered for potential up-scaled applications. The modified Ti_3C_2-MXene membranes exhibited a notable enhancement in separation performance, particularly in the removal of negatively charged dyes. Specifically, the rejections of reactive red 120 (RR120), reactive black (RB), and methyl orange (MO) dyes significantly increased from 45.2%, 40.81%, and 33.65% to 99.71%, 97.95%, and 68.91%, respectively, primarily due to the electrostatic repulsive interactions between the modified membrane surface and the negatively charged dyes.

Despite notable improvements in dye rejection compared to the pristine membrane, the separation performance of the

MXene-coated membranes in this study still lags behind the commercially available nanofiltration membranes. In addressing the observed limitation associated with the multilayered MXene structure and its impact on dye rejection efficiency, a potential avenue for improvement could involve exploring the utilization of monolayer MXenes. The monolayer MXenes offer a more compact and uniform coating layer on the membrane surface, mitigating the inherent spaces or gaps between MXene layers. This transition to a monolayer configuration could enhance the molecular separation efficiency of the MXene-coated membrane by minimizing potential pathways for dye molecules to permeate through the membrane. However, it's crucial to note that while monolayer MXene could improve the membrane performance in terms of dye rejection, transitioning to a monolayer configuration might substantially increase the overall cost of the fabricated membrane. Moreover, coating the membrane using the pressure-assisted filtration technique may result in the formation of pinholes or defects within the coated layer. Hence, investigating advanced coating methods such as 3D printing, layer-by-layer coating, chemical vapor deposition (CVD), and electrochemical deposition techniques could provide greater precision and minimize flaws. Furthermore, the selection of a binder is a critical consideration, and we recognize the necessity for further comprehensive investigations to identify a suitable binding agent that adequately fulfills the specified criteria.

The fouling performance of the ECM1 membrane, modified with Ti_3C_2-MXene, was evaluated under an electric potential using three different foulant solutions (HA, $SA/CaCl_2$, and BSA). In the case of the HA solution, applying a 4 V cathodic potential resulted in a remarkable FRR of 99.83% and a negligible decrease in FDR, while without any applied voltage, the FRR and FDR were considerably lower at 92.51% and 45.56%, respectively. Similarly, for the $SA/CaCl_2$ foulant, applying a 6 V cathodic potential increased the FRR from 84.74% to 94.4% while reducing the FDR to almost zero percent. Furthermore, when BSA was used as the model protein foulant, applying an 8 V potential to the Ti_3C_2-MXene membranes resulted in complete flux recovery (FRR of 100%) and no detectable flux decline. The observed antifouling properties of the ECM1 membranes can be mostly attributed to mechanisms such as strong electrostatic repulsive interactions and hydrogen gas bubbling through water electrolysis. These mechanisms work together to mitigate fouling and enhance the membrane's resistance to fouling.

The findings of this study provide valuable insights into the design and development of electro-conductive membranes with improved separation performance and fouling resistance. Such membranes hold promise for applications in various fields, including water treatment and filtration systems, where fouling is a critical concern. By addressing fouling challenges and offering sustainable solutions, these membranes contribute to the advancement of membrane technology and provide the potential for more efficient and environmentally friendly approaches to water treatment.

Supporting Information

Supporting Information is available from the Wiley Online Library or from the author.

Acknowledgements

The financial support for this work by the Natural Science and Engineering Research Council of Canada and Canada's Oil Sands Innovation Alliance is gratefully acknowledged.

Conflict of Interest

The authors declare no conflict of interest.

Data Availability Statement

The data that support the findings of this study are available on request from the corresponding request. The data are not publicly available due to privacy or ethical restrictions.

Keywords

antifouling, electro-conductive membranes, nanofiltration, $Ti_3C_2T_x$-MXene, wastewater treatment

Received: January 31, 2024
Revised: February 26, 2024
Published online: March 22, 2024

[1] M. Rastgar, J. Fleck, R. Graessner, A. Taghipour, M. Sadrzadeh, *J. Memb. Sci.* **2022**, *660*, 120819.
[2] M. Rastgar, A. Karkooti, A. Sohrabi, P. Karami, N. Nazemifard, M. Sadrzadeh, *Chem. Eng. J.* **2020**, *394*, 125043.
[3] M. Dadashi Firouzjaei, E. Zolghadr, S. Ahmadalipour, N. Taghvaei, F. Akbari Afkhami, S. Nejati, M. A. Elliott, *Environ. Chem. Lett.* **2021**, *20*, 661.
[4] M. D. Firouzjaei, S. F. Seyedpour, S. A. Aktij, M. Giagnorio, N. Bazrafshan, A. Mollahosseini, F. Samadi, S. Ahmadalipour, F. D. Firouzjaei, M. R. Esfahani, *J. Memb. Sci.* **2020**, *596*, 117604.
[5] M. D. Firouzjaei, M. Pejman, M. S. Gh, S. A. Aktij, E. Zolghadr, A. Rahimpour, M. Sadrzadeh, A. A. Shamsabadi, A. Tiraferri, M. Elliott, *Sep. Purif. Technol.* **2021**, *282*, 119981.
[6] M. Elimelech, W. A. Phillip, *Science* **2011**, *333*, 712
[7] M. Rastgar, A. R. Zolfaghari, H. R. Mortaheb, H. Sayahi, H. R. Naderi, *J. Adv. Oxid. Technol.* **2013**, *16*, 292.
[8] W. J. Lau, S. Gray, T. Matsuura, D. Emadzadeh, J. Paul Chen, A. F. Ismail, *Water Res.* **2015**, *80*, 306.
[9] N. Bazrafshan, M. Dadashi Firouzjaei, M. Elliott, A. Moradkhani, A. Rahimpour, *Case Stud Chem Environ Eng* **2021**, *4*, 100137.
[10] S. M. Nejad, S. F. Seyedpour, S. A. Aktij, M. D. Firouzjaei, M. Elliott, A. Tiraferri, M. Sadrzadeh, A. Rahimpour, *Mater. Today Chem.* **2022**, *24*, 100909.
[11] N. Hilal, O. O. Ogunbiyi, N. J. Miles, R. Nigmatullin, *Sep. Sci. Technol.* **2005**, *40*, 1957.
[12] M. Pejman, M. Dadashi Firouzjaei, S. Aghapour Aktij, E. Zolghadr, P. Das, M. Elliott, M. Sadrzadeh, M. Sangermano, A. Rahimpour, A. Tiraferri, *Chem. Eng. J.* **2021**, *426*, 130704.
[13] P. Karami, S. A. Aktij, B. Khorshidi, M. D. Firouzjaei, A. Asad, M. Elliott, A. Rahimpour, J. B. P. Soares, M. Sadrzadeh, *Desalination* **2022**, *522*, 115436.
[14] A. Lee, J. W. Elam, S. B. Darling, *Environ. Sci.: Water Res. Technol.* **2016**, *2*, 17.
[15] AWWA Membrane Technology Research Committee AWWA **2005**, *97*, 79.

[16] J. Kim, B. Van Der Bruggen, *Environ. Pollut.* **2010**, *158*, 2335.
[17] J. F. Li, Z. L. Xu, H. Yang, L. Y. Yu, M. Liu, *Appl. Surf. Sci.* **2009**, *255*, 4725.
[18] J. B. Li, J. W. Zhu, M. S. Zheng, *J. Appl. Polym. Sci.* **2007**, *103*, 3623.
[19] M. Pejman, M. Dadashi Firouzjaei, S. Aghapour Aktij, P. Das, E. Zolghadr, H. Jafarian, A. Arabi Shamsabadi, M. Elliott, M. Sadrzadeh, M. Sangermano, *ACS Appl. Mater. Interfaces* **2020**, *12*, 36287.
[20] M. Pejman, M. D. Firouzjaei, S. A. Aktij, P. Das, E. Zolghadr, H. Jafarian, A. A. Shamsabadi, M. Elliott, M. R. Esfahani, M. Sangermano, *J. Memb. Sci.* **2020**, *611*, 118352.
[21] L. Zhu, H. Song, G. Wang, Z. Zeng, Q. Xue, *J. Memb. Sci.* **2018**, *549*, 515.
[22] J. Liu, N. Wang, L. J. Yu, A. Karton, W. Li, W. Zhang, F. Guo, L. Hou, Q. Cheng, L. Jiang, D. A. Weitz, Y. Zhao, *Nat. Commun.* **2017**, *8*, 2011.
[23] J. Liu, L. J. Yu, G. Yue, N. Wang, Z. Cui, L. Hou, J. Li, Q. Li, A. Karton, Q. Cheng, L. Jiang, Y. Zhao, *Adv. Funct. Mater.* **2019**, *29*, 1808501.
[24] X. Hou, Y. Hu, A. Grinthal, M. Khan, J. Aizenberg, *Nature* **2015**, *519*, 70.
[25] Z. Sheng, H. Wang, Y. Tang, M. Wang, L. Huang, L. Min, H. Meng, S. Chen, L. Jiang, X. Hou, *Sci. Adv.* **2018**, *4*, aao6724.
[26] K. Huang, P. Rowe, C. Chi, V. Sreepal, T. Bohn, K. G. Zhou, Y. Su, E. Prestat, P. B. Pillai, C. T. Cherian, A. Michaelides, R. R. Nair, *Nat. Commun.* **2020**, *11*, 1097.
[27] A. Feng, J. Yuan, *Macromol. Rapid Commun.* **2014**, *35*, 767.
[28] J. Liu, X. Xu, Y. Lei, M. Zhang, Z. Sheng, H. Wang, M. Cao, J. Zhang, X. Hou, *Adv. Mater.* **2022**, *34*, 2107327.
[29] Z. Sheng, M. Zhang, J. Liu, P. Malgaretti, J. Li, S. Wang, W. Lv, R. Zhang, Y. Fan, Y. Zhang, X. Chen, X. Hou, *Natl. Sci. Rev.* **2021**, *8*, nwaa301.
[30] R. Tabassian, J. H. Oh, S. Kim, D. Kim, S. Ryu, S. M. Cho, N. Koratkar, I. K. Oh, *Nat. Commun.* **2016**, *7*, 13345.
[31] L. Jiang, M. Rastgar, C. Wang, S. Ke, L. He, X. Chen, Y. Song, C. He, J. Wang, M. Sadrzadeh, *Sep. Purif. Technol.* **2022**, *303*, 122274.
[32] A. Karkooti, M. Rastgar, N. Nazemifard, M. Sadrzadeh, *Sci. Total Environ.* **2020**, *704*, 135365.
[33] M. Rastgar, A. Bozorg, A. Shakeri, M. Sadrzadeh, *Chem. Eng. Res. Des.* **2019**, *141*, 413.
[34] P. Formoso, E. Pantuso, G. De Filpo, F. P. Nicoletta, *Membranes* **2017**, *7*, 39.
[35] L. L. Xu, Y. Xu, L. Liu, K. P. Wang, D. A. Patterson, J. Wang, *J. Memb. Sci.* **2019**, *572*, 442.
[36] G. Yi, L. Du, G. Wei, H. Zhang, H. Yu, X. Quan, S. Chen, *J. Memb. Sci.* **2022**, *658*, 120719.
[37] B. A Braghetta, F. A. DiGiano, W. P. Ball, *J. Environ. Eng.* **1997**, *123*, 628.
[38] N. Mameda, K. H. Choo, *Electrochemical Membrane Technology for Water and Wastewater Treatment*, Elsevier, Amsterdam, **2022**, pp. 195–225.
[39] K. L. Jones, C. R. O'melia, *J. Memb. Sci.* **2000**, *165*, 31.
[40] D. Liu, X. Chen, B. Bian, Z. Lai, Y. Situ, *Front. Chem.* **2018**, *6*, 00445.
[41] D. Bell, R. Sengpiel, M. Wessling, *J. Memb. Sci.* **2020**, *594*, 117397.
[42] K. P. Katuri, N. M. S. Bettahalli, X. Wang, G. Matar, S. Chisca, S. P. Nunes, P. E. Saikaly, *Adv. Mater.* **2016**, *28*, 9504.
[43] B. Khorshidi, J. Hajinasiri, G. Ma, S. Bhattacharjee, M. Sadrzadeh, *J. Memb. Sci.* **2016**, *500*, 151.
[44] B. Khorshidi, S. A. Hosseini, G. Ma, M. McGregor, M. Sadrzadeh, *Polymer* **2019**, *163*, 48.
[45] L. Du, X. Quan, X. Fan, G. Wei, S. Chen, *J. Memb. Sci.* **2020**, *596*, 117613.
[46] C. Cuevas, D. Kim, K. P. Katuri, P. Saikaly, S. P. Nunes, *J. Memb. Sci.* **2018**, *545*, 323.
[47] M. J. Larocque, D. R. Latulippe, C. F. de Lannoy, *J. Memb. Sci.* **2021**, *620*, 118859.
[48] M. Naguib, O. Mashtalir, J. Carle, V. Presser, J. Lu, L. Hultman, Y. Gogotsi, M. W. Barsoum, *ACS Nano* **2012**, *6*, 1322.
[49] M. Dadashi Firouzjaei, M. Karimiziarani, H. Moradkhani, M. Elliott, B. Anasori, *Mater. Today. Adv.* **2022**, *13*, 100202.
[50] M. Dadashi Firouzjaei, E. Zolghadr, A. Arabi Shamsabadi, M. Sadrzadeh, A. Rahimpour, F. Akbari Afkhami, E. K. Wujcik, M. Elliott, *Case Stud. Chem. Environ. Eng.* **2023**, *7*, 100296.
[51] M. Dadashi Firouzjaei, S. K. Nemani, M. Sadrzadeh, E. K. Wujcik, M. Elliott, B. Anasori, *Adv. Mater.* **2023**, *35*, 2300422.
[52] F. Seidi, A. Arabi Shamsabadi, M. Dadashi Firouzjaei, M. Elliott, M. R. Saeb, Y. Huang, C. Li, H. Xiao, B. Anasori, *Small* **2023**, *19*, 2206716.
[53] B. C. Wyatt, A. Rosenkranz, B. Anasori, *Adv. Mater.* **2021**, *33*, 2007973.
[54] K. Rasool, R. P. Pandey, P. A. Rasheed, S. Buczek, Y. Gogotsi, K. A. Mahmoud, *Mater. Today* **2019**, *30*, 80.
[55] A. Grube, A. A. Shamsabadi, M. D. Firouzjaei, S. I. G. P. Mohamed, L. Hilger, M. Elliott, K. McKenzie, M. Bavarian, *Nano Trends* **2023**, *3*, 100014.
[56] J. Gao, Y. Feng, W. Guo, L. Jiang, *Chem. Soc. Rev.* **2017**, *46*, 5400.
[57] J. Gao, A. R. Koltonow, K. Raidongia, B. Beckerman, N. Boon, E. Luijten, M. Olvera De La Cruz, J. Huang, *Mater. Chem. Front.* **2018**, *2*, 475.
[58] J. Lao, R. Lv, J. Gao, A. Wang, J. Wu, J. Luo, *ACS Nano* **2018**, *12*, 12464.
[59] K. Raidongia, J. Huang, *J. Am. Chem. Soc.* **2012**, *134*, 16528.
[60] M. Carey, M. W. Barsoum, *Mater. Today Adv.* **2021**, *9*, 100120.
[61] J. T. Lee, B. C. Wyatt, G. A. Davis Jr., A. N. Masterson, A. L. Pagan, A. Shah, B. Anasori, R. Sardar, *ACS Nano* **2021**, *15*, 19600.
[62] A. Shayesteh Zeraati, S. A. Mirkhani, P. Sun, M. Naguib, P. V. Braun, U. Sundararaj, *Nanoscale* **2021**, *13*, 3572.
[63] M. Akhlaq, U. Mushtaq, S. Naz, M. Uroos, *RSC Adv.* **2023**, *13*, 5723.
[64] C. J. Van Oss, *Interfacial Forces in Aqueous Media*, 2nd ed., Taylor and Francis, London **2006**.
[65] A. Maiti, M. Sadrezadeh, S. Guha Thakurta, D. J. Pernitsky, S. Bhattacharjee, *Energy Fuels* **2012**, *26*, 5604.
[66] J. A. Brant, A. E. Childress, *J. Memb. Sci.* **2002**, *203*, 257.
[67] M. Rastgar, A. Shakeri, A. Bozorg, H. Salehi, V. Saadattalab, *Appl. Surf. Sci.* **2018**, *441*, 923.
[68] Q. Zhang, B. Liu, G. Gao, C. D. Vecitis, *J. Phys. Chem. B* **2022**, *127*, 3164.
[69] H. He, Z. Zhou, *Crit. Rev. Environ. Sci. Technol.* **2017**, *47*, 2100.
[70] L. P. Yu, L. Lu, X. H. Zhou, L. Xu, *Adv. Mater. Interfaces* **2023**, *10*, 2201818.
[71] Z. Ling, C. E. Ren, M. Q. Zhao, J. Yang, J. M. Giammarco, J. Qiu, M. W. Barsoum, Y. Gogotsi, *Proc. Natl. Acad. Sci. USA* **2014**, *111*, 16676.
[72] K. Liu, Y. Tian, L. Jiang, *Prog. Mater. Sci.* **2013**, *58*, 503.
[73] A. Sarycheva, Y. Gogotsi, *Chem. Mater.* **2020**, *32*, 3480.
[74] J. Halim, K. M. Cook, M. Naguib, P. Eklund, Y. Gogotsi, J. Rosen, M. W. Barsoum, *Appl. Surf. Sci.* **2016**, *362*, 406.
[75] M. R. Lukatskaya, J. Halim, B. Dyatkin, M. Naguib, Y. S. Buranova, M. W. Barsoum, Y. Gogotsi, *Angew. Chem.* **2014**, *126*, 4977.
[76] S. Myhra, J. A. A. Crossley, M. W. Barsoum, *J. Phys. Chem. Solids* **2001**, *62*, 811.
[77] S. Yamamoto, H. Bluhm, K. Andersson, G. Ketteler, H. Ogasawara, M. Salmeron, A. Nilsson, *J. Phys. Cond. Matter* **2008**, *20*, 184025.
[78] T. Liu, X. Liu, N. Graham, W. Yu, K. Sun, *J. Memb. Sci.* **2020**, *593*, 117431.
[79] B. Sun, X. Dong, H. Li, Y. Shang, Y. Zhang, F. Hu, S. Gu, Y. Wu, T. Gao, G. Zhou, *Sep. Purif. Technol.* **2021**, *272*, 118964.
[80] X. Y. Ma, T. T. Fan, G. Wang, Z. H. Li, J. H. Lin, Y. Z. Long, *Compos. Commun.* **2022**, *29*, 101017.
[81] T. F. Ajibade, H. Tian, K. Hassan Lasisi, Q. Xue, W. Yao, K. Zhang, *Sep. Purif. Technol.* **2021**, *275*, 119135.

[82] M. Lu, W. Han, H. Li, W. Zhang, B. Zhang, *J Energy Chem* **2020**, *48*, 344.
[83] Q. Zhang, C. D. Vecitis, *J. Memb. Sci.* **2014**, *459*, 143.
[84] Q. Zhang, J. Wang, C. D. Vecitis, *J. Memb. Sci.* **2021**, *620*, 118803.
[85] N. Subhi, A. R. D. Verliefde, V. Chen, P. Le-Clech, *J. Memb. Sci.* **2012**, *32*, 403.
[86] S. Hong, M. Elimelech, *J. Memb. Sci.* **1997**, *132*, 159.
[87] S. Kim, E. M. V. Hoek, *Desalination* **2007**, *202*, 333.
[88] A. Subramani, X. Huang, E. M. V. Hoek, *J. Colloid Interface Sci.* **2009**, *336*, 13.
[89] E. Soheyli, D. Azad, R. Sahraei, A. A. Hatamnia, A. Rostamzad, M. Alinazari, *Colloids Surf B Biointerfaces* **2019**, *182*, 110389.
[90] J. A. Brant, A. E. Childress, *J. Memb. Sci.* **2004**, *241*, 235.
[91] R. Beckett, N. P. Le, *Colloids Surf.* **1990**, *44*, 35.
[92] J. S. Park, H. J. Lee, S. J. Choi, K. E. Geckeler, J. Cho, S. H. Moon, *J. Colloid Interface Sci.* **2003**, *259*, 293.
[93] G. C. C. Yang, C. J. Li, *Sep. Purif. Technol.* **2007**, *58*, 159.
[94] T. M. Qaisrani, W. M. Samhaber, *Desalination* **2011**, *266*, 154.
[95] Z. Zhang, G. Huang, Y. Li, X. Chen, Y. Yao, S. Ren, M. Li, Y. Wu, C. An, *Chem. Eng. J.* **2022**, *427*, 131987.
[96] Q. Gu, T. C. A. Ng, Y. Bao, H. Y. Ng, S. C. Tan, J. Wang, *Chem. Eng. J.* **2021**, *428*, 130456.
[97] Y. Liu, Y. Ren, S. You, *Electrochemical Membrane Technology for Water and Wastewater Treatment*, Elsevier, Amsterdam **2022**, pp. 111–140.
[98] G. V. Buxton, C. L. Greenstock, W. P. Helman, A. B. Ross, *J. Phys. Chem. Ref. Data* **1988**, *17*, 513.
[99] E. Brillas, A. Maestro, M. Moratalla, J. Casado, *J. Appl. Electrochem.* **1997**, *27*, 83.
[100] E. Brillas, I. Sirés, M. A. Oturan, *Chem. Rev.* **2009**, *109*, 6570.